nature communications

Article

https://doi.org/10.1038/s41467-024-51179-y

Chiral 3D structures through multi-dimensional transfer printing of multilayer quantum dot patterns

Received: 3 January 2024

Accepted: 31 July 2024

Published online: 14 August 2024

Check for updates

Geon Yeong Kim[1,4], Shinho Kim[2,4], Ki Hyun Park[1], Hanhwi Jang[1], Moohyun Kim[1], Tae Won Nam[1], Kyeong Min Song[1], Hongjoo Shin[1], Yemin Park[1], Yeongin Cho[1], Jihyeon Yeom[1], Min-Jae Choi[3] ✉, Min Seok Jang[2] ✉ & Yeon Sik Jung[1] ✉

Three-dimensional optical nanostructures have garnered significant interest in photonics due to their extraordinary capabilities to manipulate the amplitude, phase, and polarization states of light. However, achieving complex three-dimensional optical nanostructures with bottom-up fabrication has remained challenging, despite its nanoscale precision and cost-effectiveness, mainly due to inherent limitations in structural controllability. Here, we report the optical characteristics of intricate two- and three-dimensional nanoarchitectures made of colloidal quantum dots fabricated with multi-dimensional transfer printing. Our customizable fabrication platform, directed by tailored interface polarity, enables flexible geometric control over a variety of one-, two-, and three-dimensional quantum dot architectures, achieving tunable and advanced optical features. For example, we demonstrate a two-dimensional quantum dot nanomesh with tuned subwavelength square perforations designed by finite-difference time-domain calculations, achieving an 8-fold enhanced photoluminescence due to the maximized optical resonance. Furthermore, a three-dimensional quantum dot chiral structure is also created via asymmetric stacking of one-dimensional quantum dot layers, realizing a pronounced circular dichroism intensity exceeding 20°.

Periodically arranged subwavelength photonic nanostructures offer light manipulation capabilities beyond those of conventional optical components. By harnessing enhanced light scattering within a unit cell of photonic nanostructures and multiple scattering in a periodically arranged ensemble, these structures allow for precise control over amplitude, phase, and polarization of propagating light, enabling various functionalities such as frequency-selective absorption[1], wavefront shaping[2], and polarization modulation[3] based on light-matter interactions. Recently, the exploration of three-dimensional (3D) photonic nanostructures has gained momentum[4–6], surpassing the capabilities of their two-dimensional (2D) counterparts, due to their unique potential for significantly enhanced optical properties through intensified light confinement and versatile design possibilities.

Usually, 3D photonic nanostructures require designs that maximize light-matter interaction, which often entails the fabrication of intricate 3D shapes. Therefore, top-down lithography has predominantly been utilized for creating 3D photonic nanostructures, which come with complex processing requirements and limited

[1]Department of Materials Science and Engineering, Korea Advanced Institute of Science and Technology (KAIST), 291 Daehak-ro, Yuseong-gu, Daejeon, Republic of Korea. [2]School of Electrical Engineering, Korea Advanced Institute of Science and Technology (KAIST), 291 Daehak-ro, Yuseong-gu, Daejeon, Republic of Korea. [3]Department of Chemical and Biochemical Engineering, Dongguk University, Pildong-ro 1-gil, Jung-gu, Seoul, Republic of Korea. [4]These authors contributed equally: Geon Yeong Kim, Shinho Kim. ✉e-mail: minjae.choi@dgu.ac.kr; jang.minseok@kaist.ac.kr; ysjung@kaist.ac.kr

scalability[4–10]. To address these issues, bottom-up fabrication approaches have been suggested[11,12]. For example, Liu et al. recently demonstrated a high-resolution quantum dot (QD) pattern by using photoexcitation-induced chemical bonding[12]. However, the light manipulation capability of the 3D nanostructures produced by bottom-up approaches has not yet reached the level of those fabricated with top-down lithography. For example, circular dichroism (CD)–the differential extinction of left- and right-handed circularly polarized light (CPL)–is often restricted to a few degrees in the colloidal assembly method (Suppl. Fig. 1).

Here, we introduce a strategy for constructing multi-dimensional photonic nanostructures using colloidal materials. These structures were assembled using multilayer QD patterns through high-resolution transfer printing (TP), as illustrated in Fig. 1a. This method offers the flexibility of stacking angles and precise control over the structural parameters, enabling customization of these structures for diverse photonic applications. Specifically, we designed a 2D nanomesh for enhancing wavelength-selective absorption via optical resonance (Fig. 1b). The resultant 2D QD nanomesh exhibited 8-fold photoluminescence (PL) enhancement compared to QD thin film. Furthermore, the asymmetric stacking of two layers of 1D QD patterns led to effective polarization modulation (Fig. 1c). This resulted in a superior chiroptical response, with a record-high CD intensity up to 20.5°, suggesting a promising approach for designing polarization-sensitive 3D chiral configurations.

Results

Multi-dimensional transfer printing for 3D nanoarchitectures

In a conventional TP technique, multiple stacking of QD patterns is challenging due to the collapse of structures. For the flexible control of 3D nano-architectures, we designed a new multi-dimensional transfer printing (mTP) method via polarity modulation of consisting interfacial layers employed in each step of the process. mTP as illustrated in Suppl. Fig. 2, the process consists of three key steps–coating, picking,

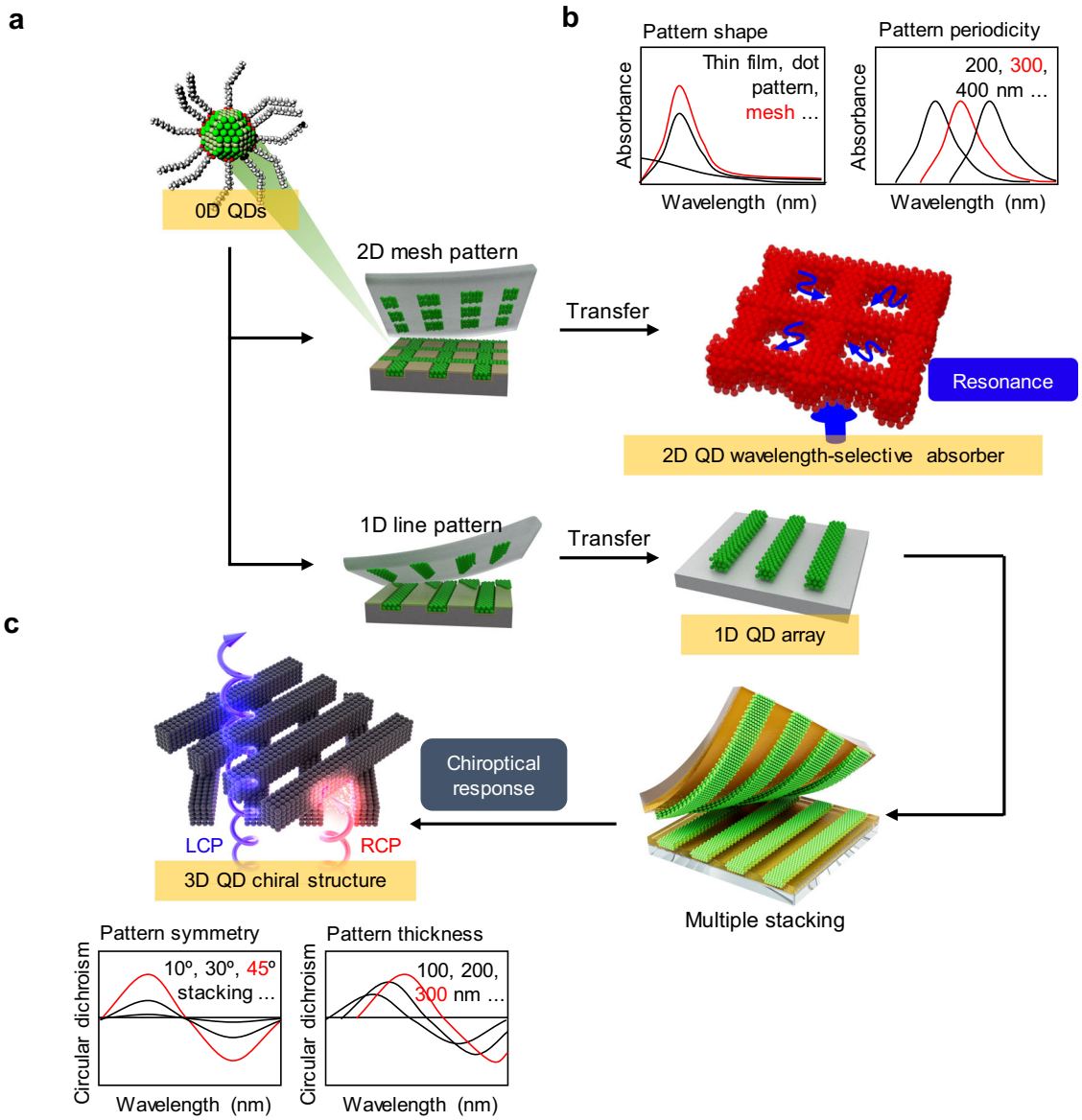

Fig. 1 | Design-driven multi-dimensional QD nano-architectures. a Schematic representation of 1D QD pattern array (green-emitting) with mTP. **b** Design for 2D QD nanostructure (red-emitting) for wavelength-selective absorption enhancement through optical resonance effects. **c** 3D Structural design of polarization-sensitive chiral nano-configurations (black color) via structural parameter control. Left- and right-handed CPL (LCP and RCP) are labeled with blue and red colors, respectively.

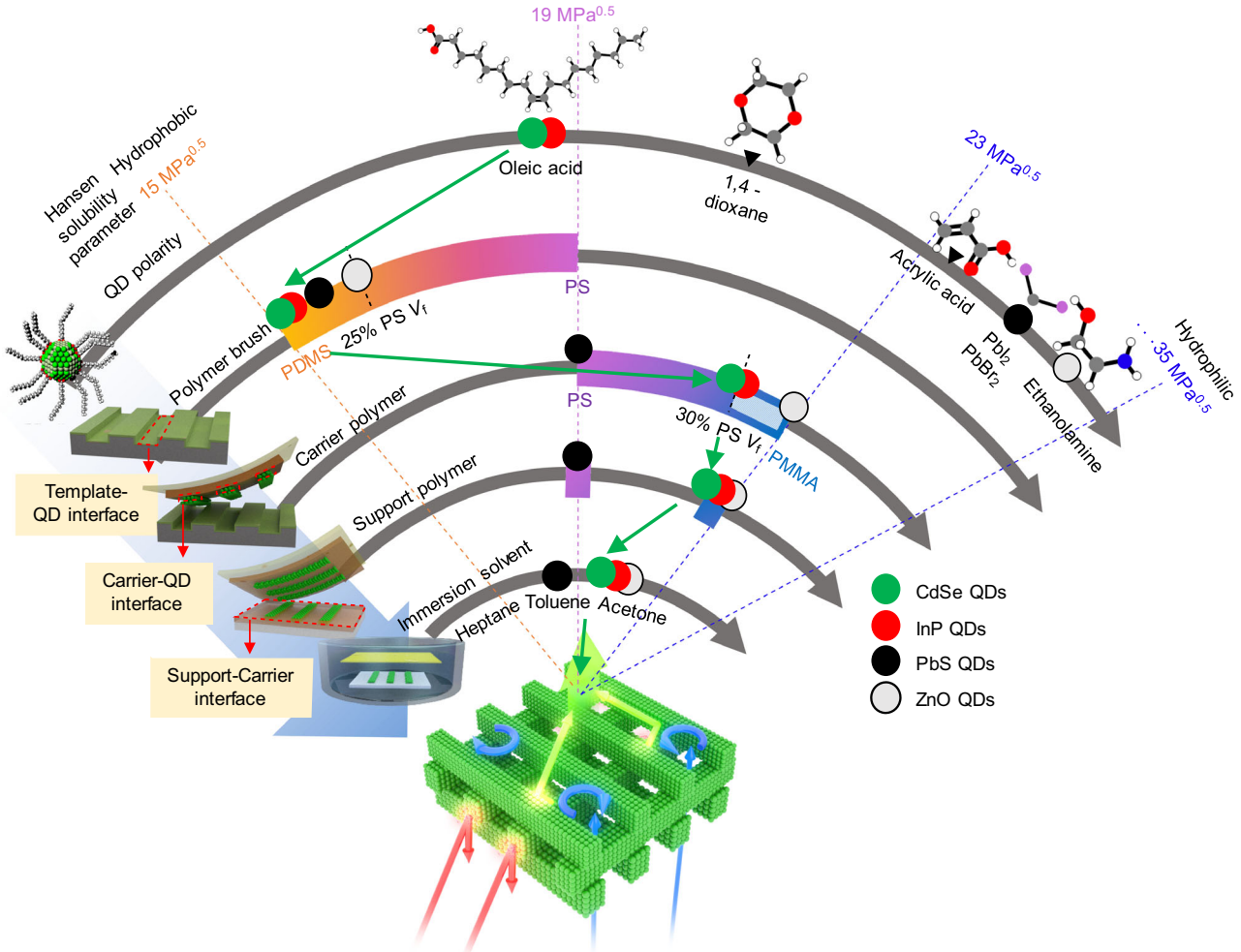

Fig. 2 | Customizable mTP process based on solubility parameters. The Hansen solubility parameters of the interface components used in mTP (ligands, brush, carrier, support polymers, and solvents) are plotted alongside the intrinsic colors of the QDs: green for CdSe, red for InP, black for PbS, and white for ZnO. The volume ratios of PDMS/PS for the brush and of PS/PMMA for the carrier are adjusted. The solubility limit of PMMA relative to PS for the carrier, marked by blue diagonal lines, stands at a 70% volume fraction (V_f).

and stacking. First, a polymer brush is coated on a pre-designed Si master template, which is composed of trench and mesa regions, to modulate the surface polarity of the template. Then, the colloidal QDs are spin-coated on the Si template. Since the QDs are coated on both the trench and the mesa regions, we developed a process to selectively remove the QDs on the mesa regions. For hydrophobic QDs, a flat polydimethylsiloxane (PDMS) mold is stamped onto the Si template. The low surface energy of PDMS favors the adhesion of the QDs over the brush-treated template, resulting in the perfect stripping of the QDs from the mesa domain (Suppl. Fig. 3). In the case of hydrophilic QDs, the PDMS mold is treated with O_2 plasma before stamping, thereby rendering the mold surface hydrophilic by forming silanol groups[13] (Suppl. Fig. 4).

The picking step, which involves the transfer of QD patterns from the trench region to the carrier substrate, determines the overall yields and dimensions of TP techniques. To securely detach the QDs from the Si template, homopolymers such as poly(methyl methacrylate) (PMMA) were spin-coated on the QDs as a carrier polymer. A polyimide (PI) adhesive film (Kapton tape) was then laminated on the homopolymer layer followed by peeling of the QDs from the Si template. However, as previously reported[14,15], our earlier TP techniques exhibited a capability of transferring QDs with thicknesses of only a few tens of nanometers (Suppl. Fig. 5c). This is due to a limited QD picking yield, as evidenced by the remaining QDs on the Si template after the picking step (Suppl. Figs. 6a, b). We thus reasoned that unbalanced wetting properties between the homopolymer and QDs resulted in the limited picking yield.

To enhance the picking yield, we, therefore, introduced a composite carrier polymer on the QDs to induce a favorable energetic compatibility between the carrier polymer and QDs (Suppl. Fig. 6e). This enabled the formation of conformal interface contact between QDs and the carrier polymer (Suppl. Fig. 7), leading to the complete removal of QDs on the Si template after the picking step (Suppl. Figs. 6c, d). As a result, we achieved a significantly extended height of transferred QDs, reaching up to 450 nm by employing mTP (Suppl. Fig. 5b). More details on interfacial energy control will be discussed subsequently with Fig. 2.

After the picking step, the QD patterns on the carrier polymer were transferred onto the target substrate and then immersed in a solvent. The immersion step promoted the dissolution of the carrier polymer, resulting in the selective transfer of the QD patterns onto the target substrate. To construct a 3D QD structure, layer-by-layer stacking was employed (Suppl. Fig. 5a). We noted that direct stacking of a thick 2D layer (over 100 nm) resulted in a collapsed structure, as shown in Suppl. Fig. 5e. To prevent this issue, an additional support polymer layer was spin-coated on the first layer of QD patterns, followed by O_2 plasma treatment to control the thickness of the support polymer layer (Suppl. Fig. 8). This support polymer layer served as a

robust framework, enabling the sequential stacking of patterns and thus realizing the 3D building blocks of QD structures with symmetry control. The resultant 3D architecture exhibited a fully suspended structure with minimal structural defects, leading to a 5-fold enhancement in PL compared to the single-layer structure (Suppl. Fig. 9). In contrast, the collapsed structure demonstrated a less significant increase (3-fold) in PL due to the structural degradation.

Interfacial energy matching in mTP

To verify the mTP technique as a universal platform, we studied different types of QDs, ranging from hydrophobic to hydrophilic. We hypothesized that the customization of the interfacial energy between the QDs and the interface layers (polymer brush, carrier polymer, and support polymer) would play a critical role in the mTP process. To quantify the surface energy of each interface component and to represent the polarities of all intermediates, we used the Hansen solubility parameters, as shown in Fig. 2. In the mTP, the overall process window is defined by the Hansen solubility parameters. To maximize the efficiency of mTP, it is critical to tune the Hansen solubility parameters for the polymer brush, carrier polymer, support polymer, and immersion solvent depending on the polarity of the QDs. These parameters should be precisely aligned within the process window to ensure optimal mTP performance.

The polarity of the QDs is determined by their surface ligands, which include oleic acid (OA) for hydrophobic CdSe QDs and InP QDs, lead iodide (PbI_2) for amphiphilic PbS QDs, and ethanolamine (ETA) for hydrophilic ZnO QDs. The polarity of different QDs was evaluated using contact angle measurements, as provided in Suppl. Fig. 10. In mTP, the polarity of the given QDs determines the material choice of the subsequent layers, allowing the rest of the process to match their interfacial energy with the QD patterns. The colored circles representing the intrinsic colors of corresponding QDs in Fig. 2 indicate the interface layers that can be selected depending on the polarity of the QDs.

The brush polymer must have a lower surface energy than the QDs to facilitate the detachment of the QDs from the Si template. For example, with OA-capped hydrophobic CdSe QDs, the polystyrene (PS) brush resulted in an almost zero picking yield due to the similar surface energy between the QDs and the PS brush (CdSe system in Suppl. Figs. 11a, b). By decreasing the surface energy of the brush polymer, the picking yield of the CdSe QDs increased, and almost 100% picking yield was achieved with the use of a PDMS brush layer. In contrast, hydrophilic ZnO QDs (ZnO system in Suppl. Figs. 11a, c) could not be spin-coated on the PDMS brush substrate due to the much higher surface energy of ZnO (Suppl. Fig. 11c). However, the incorporation of PS into the PDMS brush improved the wettability of colloidal QDs on the substrate by increasing the surface energy of the customized brush, although too high surface energy of the brush can hinder the picking of QD patterns. Both uniform coating of colloidal ZnO QDs and a near 100% picking yield were achieved with a brush composition of 25% PS volume fraction (V_f) in PDMS.

The carrier polymer is then selected to meet the following conditions which are: (1) the surface energy difference between the carrier polymer and the brush layer should be large enough to maximize the picking yield of the QDs, (2) similar surface energy between the carrier polymer and the QDs is required for strong adhesion between them (Suppl. Figs. 11d, e). The systematic control of both interfacial energy terms based on composite polymers is a prerequisite for the extensive thickness control of mTP. However, when the surface energy between the carrier polymer and the QDs was too similar, a solvent with a similar Hansen solubility parameter had to be used for spin-coating. This caused the QD pattern to re-dissolve during the spin-coating of the carrier polymer. Thus, the carrier polymer of 30% PS in PMMA provided the optimal mTP results for OA-capped hydrophobic CdSe QDs (Suppl. Fig. 11e).

Integrity of 3D QD nano-architectures obtained by mTP

The enhanced transfer yield and controllability of mTP process allow for the 3D stacking of QDs with a programmed angle, periodicity, and structure width. As an example, the 3D QD architectures featuring regularly arranged components exhibit wavelength-selective enhancements, enabling precise control over light reflection and absorption through trapping effects, as well as light extraction via scattering effects (as indicated in the scheme of (Fig. 2). Figure 3 demonstrates 2D and 3D nanostructures achieved using mTP with different types of QDs. To enable mTP to create QD structures that interact effectively within the visible wavelengths, we used a Si master template with a line pattern that has a pitch of 600 nm. The 3D QD nanostructures were uniformly fabricated by mTP over an area of several centimeters, as shown in the insets of Fig. 3. In addition, each QD layer can be stacked at arbitrary angles, allowing for the tuning of the 3D structural symmetry, as shown in the PbS QD nanostructures (Fig. 3c). Each QD layer can achieve thicknesses of several hundred nanometers, which allows for the creation of 3D structures ranging from nanometer to micrometer dimensions, marking a notable improvement over traditional TP techniques.

The structural uniformity and defects of the QD structures fabricated by mTP were investigated. SEM images in Suppl. Fig. 12 shows that the two-layer (2 L) CdSe QD nanostructure exhibits extremely rare vacancy defects in a large area over 400 μm^2, as evidenced by the clear dot patterns in the Fast Fourier Transform (FFT) image. The minimal structural defects in this structure can be attributed to the use of minimum pressure and an etching-free fabrication process offered by the mTP technique. Consequently, the high pattern quality of the Si master template is preserved and accurately transferred to the printed QD patterns, ensuring precise reproduction with minimal defects.

The transfer yield of the single-layer (1 L) QD nanostructure was calculated by counting the normal and defective pixels, utilizing the distinctive contrast between normally transferred lines and defective areas. Consequently, as shown in Suppl. Fig. 13a, the transfer yield for 1 L nanostructures of various QDs under optimized conditions was analyzed and confirmed to be close to 100%.

Furthermore, we compared QD structure constructed by mTP with the structures fabricated by the conventional transfer printing techniques: kinetics-assisted transfer printing[16] and solvent vapor-assisted transfer[14]. mTP structures exhibited significantly lower linewidth roughness (LWR) and line-edge roughness (LER) compared to the structures fabricated by the conventional transfer printing methods (Suppl. Figs. 13b, c). The LWR and LER values obtained from mTP structures were almost comparable to those of the Si template: the LWR/width of the line (W_L) and LER/W_L were 2.4% and 1.7%, respectively, for mTP structures, while the LWR/W_L and LER/W_L were 1.5% and 1.0%, respectively, for the Si master template. These LWR/W_L and LER/W_L meet the requirements of the semiconductor industry (less than 8-10% of LWR/W_L and LER/W_L), which suggests the potential of mTP technique for applications in other established industry devices.

In contrast, the kinetics-assisted transfer printing produced the QD structures only with thicknesses in the range of tens of nanometers and exhibited collapsed structures after 3D stacking due to the high pressure required during the printing (Suppl. Fig. 14). Similarly, the conventional solvent vapor-assisted transfer method, which relies on solvent swelling of carrier polymers with solvents, resulted in structure deformation because the carrier polymer became mobile during the swelling process (Suppl. Fig. 15).

Wavelength-selective 2D light absorber

Subwavelength patterning can imbue a QD structure with desired optical properties. For example, a nanopatterned QD color filter, which downconverts high-energy photons into low-energy photons, can be much more efficient in both the shorter-wavelength absorption and the longer-wavelength emission and thus result in a substantial PL

https://doi.org/10.1038/s41467-024-51179-y

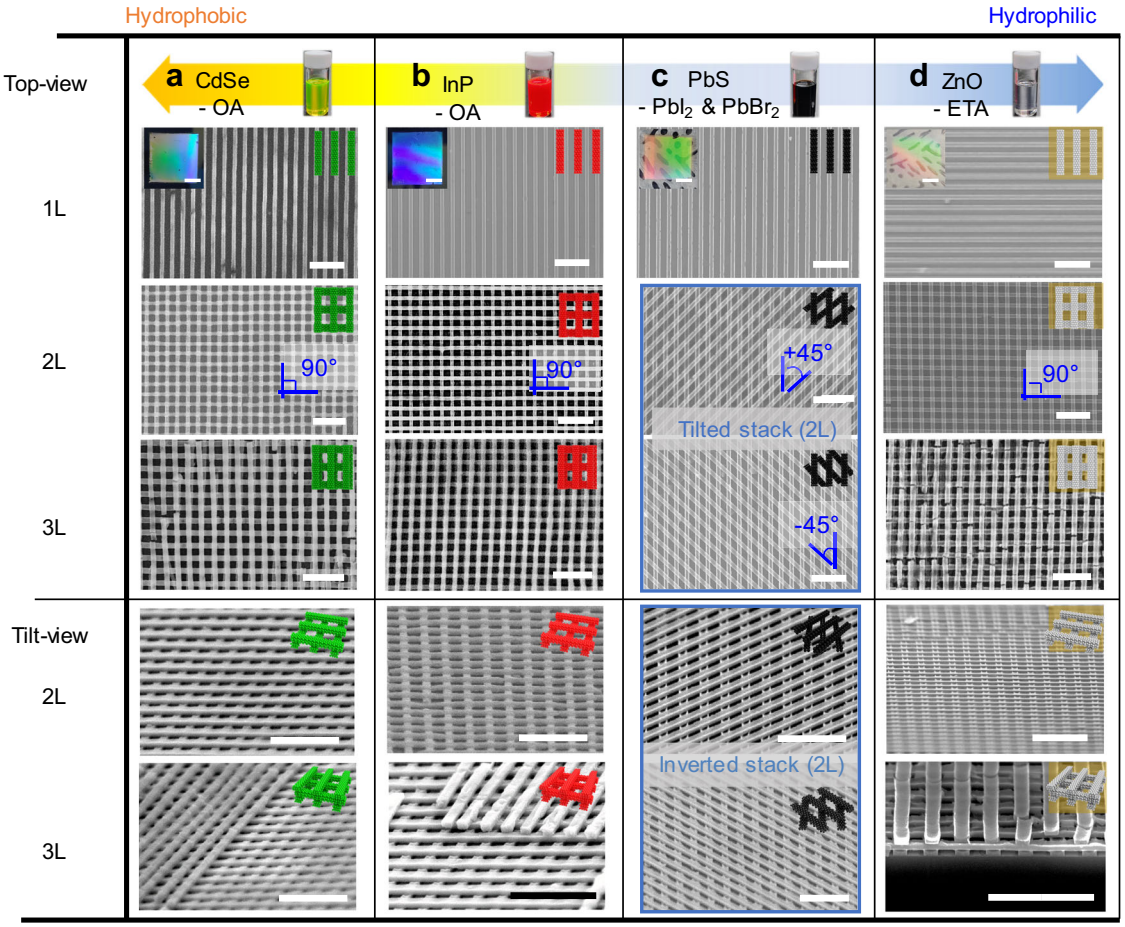

Fig. 3 | Fabrication of high-quality QD architectures. SEM images of nanostructures fabricated by mTP, representing single- to multi-layer (1 L–3 L) structures with different QDs: (**a**) CdSe, (**b**) InP, (**c**) PbS, and (**d**) ZnO. The SEM images highlighted with blue solid lines indicate PbS nanostructures stacked at tilted and inverted angles. Scale bars for the SEM images and the insets are 2 μm and 5 mm, respectively.

enhancement compared to conventional thin QD films[17,18]. In this work, we sought to design an optimal photonic nanostructure that maximizes absorption at 450 nm of excitation light. Here, the optimization process was performed for thick photonic nanostructure, which is advantageous for effective light confinement (refer to Suppl. Fig. 16; compared to the thin nanostructures prepared via conventional TP methods, the thicker structures obtained by our mTP method are advantageous for achieving effective light confinement, hence, for high absorption enhancement).

Figure 4b presents the numerically calculated spectra of absorption enhancement factors (E_{450}) depending on various pattern shapes including square, triangular, and circular patterns. The highest enhancement factor was observed for the inverted patch pattern, exhibiting an E_{450} value of 2.7. The enhancement factor was calculated as a function of the periodicity and the QD filling ratio of the inverted patch structure (Fig. 4c). The results reveal that the highest absorption enhancement can be achieved with a periodicity of 306 nm and a QD filling ratio of 48%. Considering all the calculation results, we concluded the optimal geometry of E_{450} for green and red CdSe QDs illustrated in Fig. 4a. To reveal the origin of significant absorption enhancement at 450 nm, we calculated the photonic band structure of the optimized mesh array[19] (Fig. 4d). A degenerate band-edge mode at the Gamma-point was observed with a normalized frequency of 0.68, which is well matched to the resonance peak wavelength (450 nm) of the optimized mesh structure. This Gamma-point band-edge mode enhances light-matter interaction due to the slow group velocity at the symmetry point[20]. The calculated out-of-plane electric field component (E_z) profile of the Gamma-point band-edge mode depicts that the transverse magnetic (TM)-like electric field is tightly confined in the QD area.

We then programmed the QD structures based on the theoretical calculation results by using a mesh-patterned Si template (Suppl. Fig. 17), resulting in high-quality QD mesh structures as shown in SEM images (Fig. 4f, g). A significant PL enhancement was experimentally observed in both green and red QD mesh structures compared to the QD thin films, exhibiting enhancement factors of 7.8 and 5.6, respectively (Fig. 4k). Inductively coupled plasma mass spectrometry (ICP-MS) analysis revealed that both the QD mesh structures and the QD thin films contain similar amounts of QDs, indicating that the PL enhancements of the QD mesh structures originate from the effect of photonic structures (Suppl. Table 1).

To understand the contributing factors to PL enhancement, we examined absorption (Fig. 4i,l) and extraction (Fig. 4j, m) in the green and red mesh patterns using finite-difference time-domain (FDTD) calculations. The values for all these factors are included in Suppl. Table 2. The calculated absorption spectra of the mesh patterns (Fig. 4i, l) exhibit resonance peaks close to the blue color-frequency, indicating enhanced absorption through light confinement effects. The measured absorption spectra (Suppl. Fig. 17) closely match the calculated spectra, with slightly lower maximum absorption at the resonance frequencies, possibly due to rounded edges and small size deviations in the template structures fabricated through e-beam lithography (Suppl. Fig. 18).

Regarding extraction, despite the significant difference between the emission wavelength of the QDs and the resonance wavelength of the structure, the mesh pattern exhibits higher extraction efficiency

https://doi.org/10.1038/s41467-024-51179-y

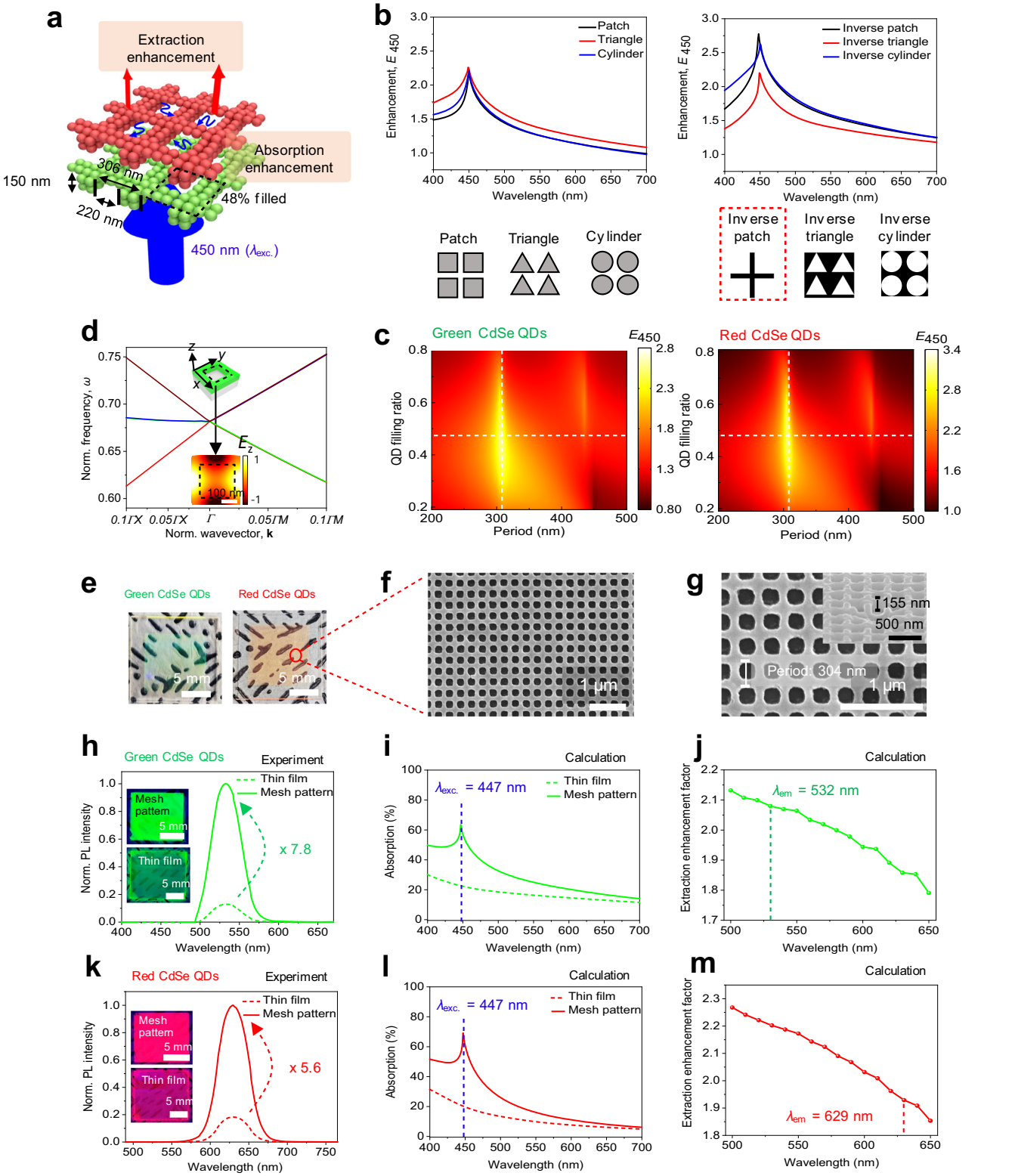

compared to the thin film (Fig. 4j, m). This enhanced extraction in the mesh pattern is attributed to the grating diffraction effect[21], whereas the thin film experiences hindered extraction due to total internal reflection. Additionally, our mesh pattern shows significantly higher emission at an angle of 45° compared to other angles due to structural effects (Suppl. Fig. 19). The emission intensity at 45° is comparable to the front 90° emission, which is crucial for practical display applications. These findings demonstrate the angle-dependent emission control capability for metamaterial applications using our tunable and precise design tool.

We also investigated the degradation of the optical properties of the QDs during mTP process. PL quantum yield (QY) of the QD solution, QD thin film, and the QD structure fabricated by mTP were compared in the case of red CdSe QDs (Suppl. Fig. 20). This reveals that the QDs retain their emission properties during mTP process, suggesting that mTP process does not cause any physical and chemical

Fig. 4 | Wavelength-selective 2D light absorber. a Design of a multilayer QD nanomesh for enhanced absorption at 450 nm wavelength and improved extraction of emitted light. The illustration indicates green- and red-QD-mesh structures (pitch 306 nm, width 86 nm, and height 150 nm). **b** Calculated E_{450} (enhancement spectra for light absorption at 450 nm, compared to thin films) for different-shaped nanopatterns. The insets below present the unit cells of each corresponding nanostructure. **c** Calculated E_{450} spectra for different-sized nanopatterns. **b**–**c**, Optimal values for shape-dependent and size-dependent absorption are determined by varying the period and QD filling ratio while maintaining a constant nanopattern thickness of 150 nm. **d** Calculated photonic diagram for the optimized mesh structure. The frequency ω is defined as the ratio of p/λ (306 nm pitch/wavelength). The wavevector **k** is defined as the ratio of $\mathbf{k}f/p$. The lower inset shows the calculated electric field (E_z) profile of the Γ (gamma) point band-edge mode as depicted in the upper inset of the QD unit cell. **e** Optical images of the printed green- and red-QD-mesh patterns. **f**, **g** The corresponding SEM images. **g** The inset SEM image shows a tilt-view image of the pattern. **f**, **g** The printed pattern has a 205 nm line width and a 102 nm space width on average, with a deviation of only 7 nm from the fabricated template. **h**, **k** PL ($\lambda_{exc.}$ = 442 nm) comparison results for the thin films and (**h**) green- and (**k**) red-QD-mesh patterns. The inset images show the emission color under UV light ($\lambda_{exc.}$ of 325 nm). **i**, **l** Absorption spectra of thin films and (**i**) green- and (**l**) red-QD-mesh patterns. The dotted lines indicate the resonance peaks of the mesh structures. **j**, **m** Emission wavelength-dependent extraction efficiencies of (**j**) green- and (**m**) red-QD-mesh patterns. The total extraction efficiencies of the mesh patterns were divided by those of the films. The dotted lines indicate the emission wavelengths of the green- and red-mesh structures.

damage to the transferred materials. In contrast, the degradation of PL QY was observed without the use of the carrier polymer during mTP process, implying the effective passivation against chemical degradation by the carrier polymers during the immersion process[15].

CPL-sensitive 3D chiral nanoarchitecture

Optical chiral structures, characterized by their twisted or spiraled configurations, selectively absorb one form of CPL, making them highly useful in chiroptical biosensing and diagnostic tools—such as chiral drug discrimination in the pharmaceutical industry[22]. A high CD, denoting a substantial absorption disparity between LCP and RCP, is vital for effective chiral discrimination in applications such as chiral sensing, optical communications, and biomedical diagnostics. With a proper designing and fabrication tool for the chiral structures, a systematic modulation of handedness and CD peak position[3,23–25], is crucial for quantitative analyzes. Advanced fabrication techniques, including both bottom-up and top-down approaches, have been employed to achieve tunable CD properties.

Fabricating a 3D configuration with a sufficiently high thickness is of great importance for realizing highly responsive chiral nanostructures. This is because CPL, which is intrinsically a 3D form, tends to interact more effectively with 3D nanostructures. This explains why metamaterials[26] have been spotlighted in the aspects of high response to CPL[3,27–30]. However, despite diverse approaches such as colloidal assembly[3,24,31], and nanosphere[27]/micellar[32]/laser[28]/e-beam lithography[30,33], technical challenges have hindered the achievement of structural requirements for high-thickness (> hundreds of nanometers) 3D chiral structures.

To this end, we designed simple chiral nanostructures composed of cross-stacked QD grating patterns, as illustrated in the inset of Fig. 5a. As already shown in Fig. 3c, mTP is capable of fabricating 3D twisted nanoarchitectures made solely of PbS QDs, with layer thicknesses of up to 450 nm, thereby enabling a high CPL absorption capacity. The flexible angle controllability between crossed QD grating patterns offered by mTP can create various asymmetric geometries for high chirality. Additionally, the extensive control over structural parameters, such as symmetry, dimension, and thickness, allows for tunable CD spectra as will be demonstrated below.

Imparting chirality with handedness inversion is crucial for utilizing both LCP and RCP. The stacking angle can be freely controlled using mTP, which allows for easy manipulation of the handedness (Fig. 5a). In chiral media, the CD is proportional to the magnetoelectric coupling coefficient, which measures the strength of the intercoupling between electric field and magnetic field[34]. It is important to note that the magnetoelectric coupling coefficient is closely related to the mirror asymmetry of the structure. For samples stacked at a 90° angle, the image of the structure is superimposed with their mirror images, thereby lacking mirror asymmetry and resulting in minimal CD intensity. In contrast, the samples with +45° and −45° stacking angles shown in Fig. 5b exhibit mirror asymmetry, resulting in a nonzero magnetoelectric coupling coefficient. Therefore, they show significantly enhanced CD intensity, and each has nearly identical but inverse spectra. Furthermore, the +45° sample with in-plane rotation angles displayed a negligible linear dichroism (LD) (Suppl. Fig. 21), suggesting that the chirality at 45° originates from the asymmetric structure effect. The CD is closely correlated with the intrinsic absorption spectrum of PbS QDs[35,36], and the maximum CD is found near the intrinsic absorption peak at approximately 910 nm (Suppl. Fig. 22a).

To investigate the relationship between structural collapse and CD spectra, we prepared three QD structures using different TP methods: mTP, conventional TP, and conventional TP with a roll laminator. Figure 5c, d present the representative QD structures and their corresponding CD spectra, respectively. The QD structures produced using conventional TP exhibited structural collapse, which worsened with the increased pressure induced by a roll laminator. In contrast, the QD structure prepared by mTP showed no sign of collapse. This structural collapse in QD structures led to a 70% reduction in CD of the QD structure prepared by the conventional TP with a roll laminator compared to those prepared by mTP. This is attributed to the fact that the structural collapse reduces mirror asymmetry, which in turn decreases magneto-electric coupling in the structure[37]. These results emphasize the critical importance of maintaining the integrity of a perfectly suspended 3D architecture to achieve a high CD.

In Fig. 5e, f, the CD spectra of the structures, controlled in thickness and maintaining the −45° stacking configuration, are presented. The comparison between the measured and calculated CD spectra confirms a gradual increase in the magnitude of the dominant peaks as well as red-shifts of the peaks, as the thickness of the structures increases. The observed increase in CD with thickness originates from better optical mode confinement and the subsequent strong resonant magnetoelectric effect in QD structures (see Suppl. Fig. 23). On the other hand, the observed decrease in CD at the 480 nm is due to an increase in background material absorption loss of thick QD structures. Consistent with the calculation results, the samples with a grating thickness of 280 nm exhibit the maximum CD (≈ 20.5°), which is one of the highest reported values for the UV to mid-IR range. The red-shift trend can be attributed to the enhanced interaction of the 3D nanostructure with longer wavelengths as its thickness increases, a phenomenon observed in various chiral nanostructures[38].

The CD peak is influenced by the interactions between the intrinsic absorption of achiral PbS QDs and the extrinsic resonance resulting from structural effects. Consequently, variations in the resonance peak of the structure with the thickness (Suppl. Fig. 22a) can lead to corresponding variations in the CD peak. The partial discrepancy between the measured and calculated CD spectra can be attributed to multiple factors. First, the systematic methods used to calculate the CD may not perfectly align with the measurement setup, as direct absorption measurement for each LCP and RCP is not feasible in the CD spectrometer. Second, slight variations in the structural orientations of the actual samples can contribute to the observed discrepancies. As demonstrated in Suppl. Fig. 24, deviations in structural parameters such as width, thickness, penetration depth, and

https://doi.org/10.1038/s41467-024-51179-y

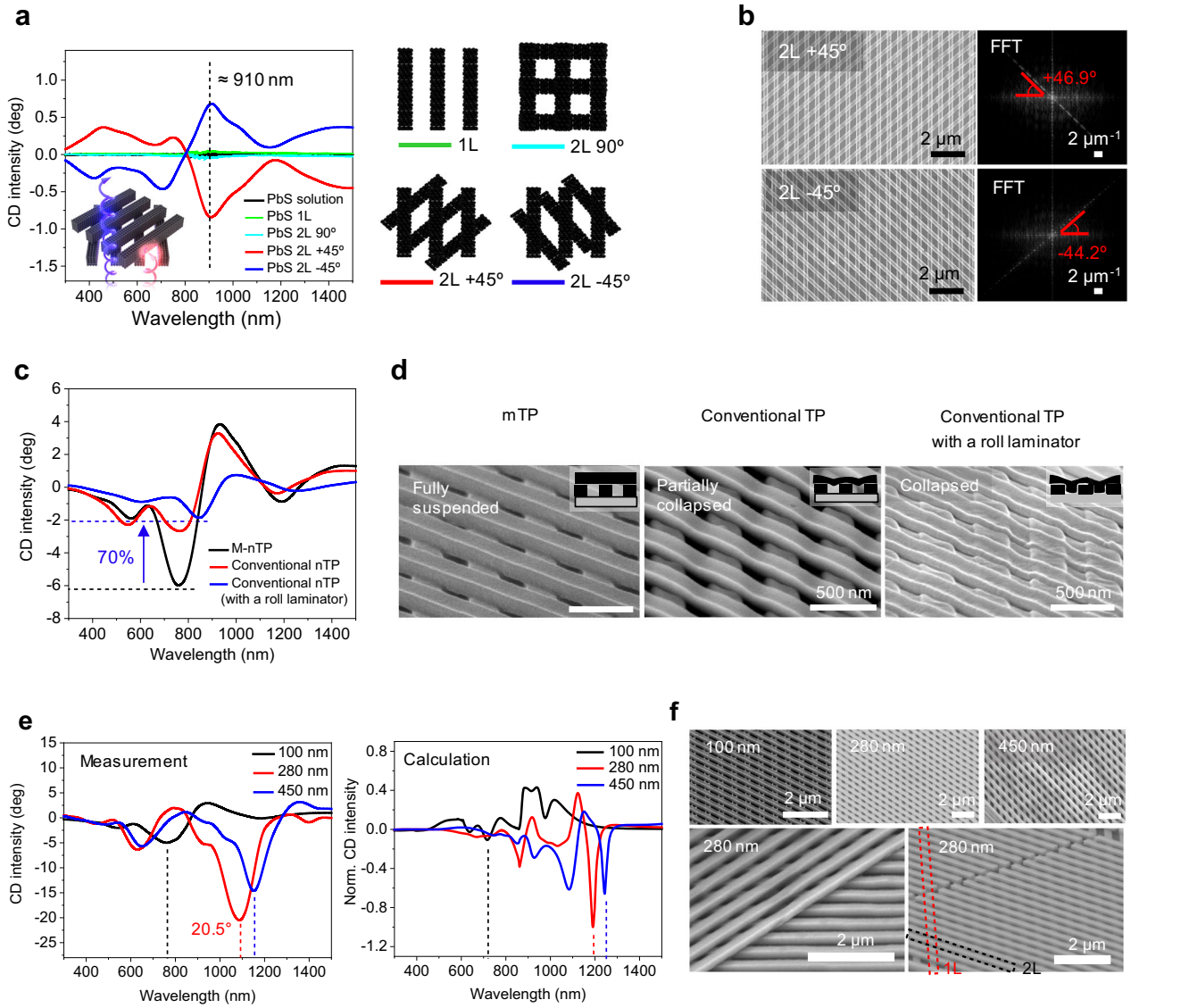

Fig. 5 | CPL-sensitive 3D chiral nanoarchitecture. a Symmetry-dependent CD spectra of PbS nanostructures. The dotted line in the spectra indicates the wavelength of maximum CD in the 45° samples. The inset of CD spectra depicts an illustration for 3D chiral nanostructure exhibiting CPL-selective interaction. Four illustrations in absorptive black color represent the geometric scheme for each sample. **b** Top-view SEM images depict the fabricated PbS 2 L 45° structures with the FFT images. A single layer of the structures has an average thickness of 65 nm. **c** Dimension-dependent CD spectra of PbS nanostructures (2 L −45°) and **d** their respective tilt-view SEM images. The absence of support polymers in conventional TP samples results in gradual structural deformation under excess pressure. Each layer of the structure has a thickness of 130 nm. **e** Thickness-dependent CD spectra (measured and calculated) of PbS structures (2 L −45°) and (**f**) their respective tilt-view SEM images. The dotted lines in each spectrum indicate the dominant peaks of each sample. **a**–**f** A single layer of PbS nanostructures has an average width of 270 nm (580 nm pitch).

stacking angles have significant effects on both the smoothness and positioning of resonance peaks in the CD spectra, which closely match the experimentally measured CD spectra. This is further evidenced by the FFT patterns of SEM images in Fig. 5b, where +45° and −45° structures reveal average angles of 46.9° and 44.2°, respectively.

The gradual decrease in CD for thicknesses above 400 nm can be explained by the diminished absorption selectivity between LCP and RCP. The absorption spectra and *g*-factor (dissymmetry factor) with the thickness modulation shown in Suppl. Fig. 22 confirms the existence of an optimum thickness for QD grating layers. Consequently, in our PbS QD-based system, an optimal grating thickness of 280 nm has been identified for achieving the highest CD. Moreover, the extensive thickness control capability provided by mTP allows for modulation of both the magnitude (up to 20.5°) and peak position (760–1150 nm) of the CD spectra in this study. This is the highest CD attained through the enhanced responsive interactions of the structure with polarized light (Suppl. Fig. 1).

Discussion

We demonstrated a highly versatile patterning platform for the fabrication of three-dimensional QD nanostructures. Owing to its adjustable construction parameters, including stacking angle, pattern periodicity, and layer thickness, we were able to produce a tailored 3D optical nanostructure exhibiting pronounced optical response. We evaluated their optical performance by fabricating 2D nano-mesh structure, which resulted in a PL enhancement of 6–8 times greater than that of conventional thin-film samples. Most notably, our 3D QD chiral structures, achieved by the tilted stacking of QD patterns, showed a CD of up to 20.5°, which is higher than the values reported for the UV to mid-IR range. Our colloidal nanomaterial-based bottom-

up approach offers a cost-effective and flexible pathway, with the reusability of the master mold, to create complex 3D photonic structures with high optical response. We anticipate that our platform, named mTP, will facilitate the development of diverse and innovative 3D optical nanostructures, providing practical and customizable functionalities.

Methods

CdSe/ZnS synthesis

Red CdSe/CdS/ZnS[39]: In a 100 mL flask under an Ar condition, 1 mmol of cadmium oxide (CdO, 99.5%), 4 mmol of OA(99.9%), and 20 mL of 1-octadecene (ODE, 90%) were added. The reactor's temperature was increased to 300 °C until the mixture turned transparent. The first stock solution, containing selenium powder (Se) and trioctylphosphine (TOP, 99.5%), was then injected into the reactor to grow the CdSe core. The temperature was maintained at 300 °C for 90 s, and 0.75 mmol of 1-dodecanethiol (DDT, 98%) was added to cover the CdS shell on the cores. After 30 min, a second stock solution was added, consisting of 4 mmol of zinc acetate ($Zn(Ac)_2$, 99.99%) and 2 mL of tributylphosphine (TBP), dissolving 4 mmol of sulfur powder (S). The mixture was reacted at the same temperature for 20 min.

Green CdSe/ZnS[40]: A mixture of zinc oxide (ZnO) and cadmium acetate ($Cd(Ac)_2$) was stirred vigorously and degassed before adding 7 mL of OA and heating the mixture at 150 °C for 30 min. Subsequently, 15 mL of ODE was added, followed by an injection of 2.5 mmol of S, 1.5 mmol of Se, and 3 mL of trioctylphosphine (TOP) to grow the core. To form a ZnS shell, 1.6 mmol of S in 2.4 mL of ODE was added to the reactor, which was then heated to 310 °C under argon conditions. After 12 min, the temperature was lowered to 270 °C, and a solution containing 3 mmol of zinc acetate dihydrate ($Zn(Ac)_2$, 98%), 1 mL of OA, and 4 mL of ODE was rapidly injected. The reactor was maintained for 20 min with the injection of a mixture of 9 mmol of S and 5 mL of TOP.

InP/ZnSe/ZnS synthesis

Red InP/ZnSe/ZnS[41]: To prepare the $In(PA)_3$ precursor, indium acetate ($In(OAc)_3$, 99.99%) and palmitic acid (PA) were dissolved in ODE to obtain a 0.2 M solution. Tris(trimethylsilyl)phosphine in trioctylphosphine (TMS_3P/TOP) solution, with a concentration of 0.2 M, was prepared separately. A 0.4 M zinc oleate ($Zn(OA)_2$) precursor was also prepared. Additionally, Se and S precursors were prepared by dissolving the Se pellet and S powder in TOP separately. To synthesize InP cores, a flask containing $In(OAc)_3$ and PA in ODE was heated, and TMS_3P/TOP was injected at 280 °C. The reaction mixture was maintained at 260 °C to obtain the desired core sizes. The InP core was then precipitated, re-dispersed in toluene, and characterized. To synthesize InP/ZnSe/ZnS QDs, we prepared a mixture of $Zn(OAc)_2$ and OA in trioctylamine (TOA, 98%). The solution was heated, and the InP core was injected, followed by adding hydrofluoric acid (HF) in acetone. The reaction mixture was further heated for the growth of ZnSe and ZnS shells.

PbS synthesis and ligand exchange[42]

PbS synthesis: A solution was prepared by dissolving 11.38 g of lead acetate ($Pb(CH_3COO)_2$, 99.999%) in a mixture of 21 mL of OA and 300 mL of ODE at 100 °C. The solution was degassed overnight and then heated to 150 °C under a nitrogen condition. Separately, the S precursor was prepared by combining 3.15 mL of hexamethyldisilathiane with 150 mL of ODE. The reaction was initiated by rapidly injecting the S precursor into the Pb precursor solution. Once the synthesis was complete, the solution was transferred into a glovebox filled with nitrogen. Methanol was added for the purification of the QDs, followed by centrifugation. The purified QDs were then re-dispersed in octane and stored within the glovebox.

PbS ligand exchange (PbI_2 and $PbBr_2$ ligands): The precursor solution was prepared by dissolving PbI_2 (99.999%, 0.1 M), $PbBr_2$ (98%, 0.02 M), and NH_4Ac (0.055 M) in 10 mL dimethylformamide (DMF). To this solution, 5 mL of the QD solution dissolved in octane (7 mg mL^{-1}) was added. The resulting solution was vigorously mixed for 1–2 min to facilitate the transfer of QDs to the DMF phase. The octane phase was then discarded, and the DMF solution was washed three times with octane. Next, the DMF solution was precipitated by adding toluene and subsequently dried under a vacuum. We then re-dispersed the resulting QD solids in butylamine (BTA) and spin-cast them onto the template in the glove box under an argon atmosphere.

ZnO synthesis[43]. A stock solution was prepared by dissolving 3 mmol of $Zn(Ac)_2$ in 30 mL of dimethyl sulfoxide (99.9%). A tetramethylammonium hydroxide (TMAH) solution was also prepared by dissolving 5 mmol in 10 mL of ethanol. The TMAH solution was then slowly injected dropwise into the stock solution at a rate of 5 mL min^{-1}, followed by stirring for 1 h at room temperature. For purification, we precipitated the reactant solution by adding acetone. After centrifugation, the solution was dispersed in 5 mL of ethanol and subjected to 5 min of sonication. The solution was then filtered through a PVDF filters (200 nm pores). Finally, ethanolamine (ETA) was injected into the solution with a volume of 80 µL.

Master template fabrications. The template of 600 P line pattern (300 nm line, 300 nm space width) was fabricated by photolithography process with a KrF scanner (Nikon S-204B), and the template of the 306 P mesh pattern (220 nm line, 86 nm space width) was fabricated by e-beam lithography with NanoBeam-nB5 followed by plasma etching.

mTP for 3D QD nanostructures. Each QD solution was cast on the template by a spin-coater, and the as-cast PbS films on the template were annealed on a hot plate at 70 °C for 5 min to ensure structural stability. The PDMS mold for the stamping was prepared with prepolymers and curing agent (Sylgard 184 from Dow Corning Co. Ltd.) which were mixed at a 10:1 weight ratio and degassed under vacuum to remove air bubbles. The mixture was then poured onto a glass mold and annealed at 140 °C for 30 min in a convection oven. The Hansen solubility parameters for various materials were obtained from the refs. 44,45. The parameters of ligands were used as the Hansen values for the corresponding QDs. We modulated the surface energy of the composite polymers corresponding to the QDs by adjusting the volume ratio of the following solutions. The brush polymers were prepared by blending a 4 wt.% hydroxyl-terminated PDMS (PDMS-OH, M_W 5 kg mol^{-1}) solution in heptane and a 4 wt.% hydroxyl-terminated PS (PS-OH, M_W 130 kg mol^{-1}) solution in toluene. The blended solution initially appeared opaque due to the phase separation of PS in heptane. Upon the addition of ≈ 50 vol.% toluene to the total solution, it underwent a transition to a transparent state. The blended solution was spin-coated on the template, and thermally treated in an oven under a vacuum for 60 min twice. The carrier polymers were made by blending a 4 wt.% PS (M_W 280 kg mol^{-1}) solution in toluene and a 4 wt.% PMMA (M_W 350 kg mol^{-1}) solution in acetone. The blended solution was spin-coated on the QD-coated template. To peel off the carrier polymer and patterns from the template, PI adhesive tape was used. The transferred patterns on the target substrate were immersed in acetone (99.9%, HPLC-grade) or toluene (99.5%) in a beaker for at least 2 h. For 3D nanostructures, the support polymers were used with either 6 wt.% PMMA (350 K) in acetone or 6 wt.% PS (280 K) in toluene. The O_2 plasma treatment was conducted with a power source of 100 W, bias power of 100 W, and duration of 165–200 s, depending on the thickness of the pattern. Subsequently, after the removal of the support polymer layer, on the previously transferred QD patterns, newly delaminated patterns attached to PI tape can be oriented controllably, as illustrated by the stacking of two-layer structures with an alignment angle of 45° or 90°.

Characterization of QD nanostructures. Cross-sectional, tilt-view, and top-view SEM images of QD nanostructures were obtained using a field emission (FE)-SEM (S4800, Hitachi). The relative degree of surface energy in PDMS mold and various QDs was compared using a contact angle analyzer (Phoenix, SEO). Quantitative analysis of critical dimensions (CD), pitch, LWR, and LER was performed using commercial image analysis software (SuMMIT) based on SEM images. PL spectra of visible-emitting QDs were measured using photoluminescence spectroscopy (MPT, PSI and Hitachi, F-7000). Diffuse transmittance and reflectance of the QD structures were measured using UV-vis spectroscopy (Solid Spec−3700, Shimadzu) to obtain absorption spectra. We measured the PL QY of QD solutions and films using a UV-NIR absolute PL QY spectrometer (C13534-11, HAMAMATSU). The compositions of QDs in the nanostructures were quantified using ICP-MS (7700 S, Agilent). An acid solution of 70% HNO_3 7 mL and 35% HCl 3 mL was used to selectively dissolve the glass substrate from the film. We utilized the J-1700 CD spectrophotometer (JASCO company) to measure the CD spectra of two-layer PbS structures over a wavelength range of 200–1600 nm.

Optical simulation. A commercial software, Lumerical FDTD, was employed to calculate light absorption, extraction, and CD. Total extraction efficiencies were calculated by averaging the ratio of outcoupled power to dipole-emitted power for orthogonally polarized electric dipole sets. The dipole sets are evenly distributed at 18 points within the region of QD materials corresponding to the irreducible first Brillouin zone. The CPL response of a thickness-dependent PbS structure was obtained by calculating the absorption for incident LCP and RCP light. The complex refractive indices of CdSe and PbS QDs were obtained from ellipsometry measurement (ALPHA-SE).

Reporting summary

Further information on research design is available in the Nature Portfolio Reporting Summary linked to this article.

Data availability

The data that support the findings of this study are available from the corresponding authors upon request. Data access is subject to institutional approval and compliance with the ethical guidelines of the corresponding institutions. Data can only be shared for non-commercial purposes and requires a data use agreement.

References

1. Lee, J., Min, K., Park, Y., Cho, K. S. & Jeon, H. Photonic crystal phosphors integrated on a blue LED chip for efficient white light generation. *Adv. Mater.* **30**, 1703506 (2018).
2. Jang, M. et al. Wavefront shaping with disorder-engineered metasurfaces. *Nat. Photonics* **12**, 84–90 (2018).
3. Probst, P. T. et al. Mechano-tunable chiral metasurfaces via colloidal assembly. *Nat. Mater.* **20**, 1024–1028 (2021).
4. Takahashi, S. et al. Direct creation of three-dimensional photonic crystals by a top-down approach. *Nat. Mater.* **8**, 721–725 (2009).
5. Chanda, D. et al. Large-area flexible 3D optical negative index metamaterial formed by nanotransfer printing. *Nat. Nanotechnol.* **6**, 402–407 (2011).
6. Liu, Y. et al. Structural color three-dimensional printing by shrinking photonic crystals. *Nat. Commun.* **10**, 4340 (2019).
7. Nelson, E. C. et al. Epitaxial growth of three-dimensionally architectured optoelectronic devices. *Nat. Mater.* **10**, 676–681 (2011).
8. Hahm, D. et al. Direct patterning of colloidal quantum dots with adaptable dual-ligand surface. *Nat. Nanotechnol.* **17**, 952–958 (2022).
9. Tang, X., Chen, M., Ackerman, M. M., Melnychuk, C. & Guyot-Sionnest, P. Direct imprinting of quasi-3D nanophotonic structures into colloidal quantum-dot devices. *Adv. Mater.* **32**, 1906590 (2020).
10. Wang, Y. et al. Diffraction-grated perovskite induced highly efficient solar cells through nanophotonic light trapping. *Adv. Energy Mater.* **8**, 1702960 (2018).
11. Abelson, A. et al. Collective topo-epitaxy in the self-assembly of a 3D quantum dot superlattice. *Nat. Mater.* **19**, 49–55 (2020).
12. Liu, S. F. et al. 3D nanoprinting of semiconductor quantum dots by photoexcitation-induced chemical bonding. *Science* **377**, 1112–1116 (2022).
13. Tang, K. C. et al. Evaluation of bonding between oxygen plasma treated polydimethyl siloxane and passivated silicon. *J. Phys.: Conf. Ser.* **34**, 155–161 (2006).
14. Jeong, J. W. et al. High-resolution nanotransfer printing applicable to diverse surfaces via interface-targeted adhesion switching. *Nat. Commun.* **5**, 5387 (2014).
15. Nam, T. W. et al. Thermodynamic-driven polychromatic quantum dot patterning for light-emitting diodes beyond eye-limiting resolution. *Nat. Commun.* **11**, 3040 (2020).
16. Kim, T. H. et al. Full-colour quantum dot displays fabricated by transfer printing. *Nat. Photonics* **5**, 176–182 (2011).
17. Lozano, G. et al. Plasmonics for solid-state lighting: enhanced excitation and directional emission of highly efficient light sources. *Light Sci. Appl.* **2**, e66 (2013).
18. Kim, G. Y. et al. Order-of-magnitude, broadband-enhanced light emission from quantum dots assembled in multiscale phase-separated block copolymers. *Nano Lett.* **19**, 6827–6838 (2019).
19. Joannopoulos, J. D. *Photonic Crystals: Molding The Flow Of Light*. (Princeton University Press, 2008).
20. Yoshida, M. et al. High-brightness scalable continuous-wave single-mode photonic-crystal laser. *Nature* **618**, 727–732 (2023).
21. Rigneault, H., Lemarchand, F., Sentenac, A. & Giovannini, H. Extraction of light from sources located inside waveguide grating structures. *Opt. Lett.* **24**, 148 (1999).
22. Lininger, A. et al. Chirality in Light-Matter Interaction. *Adv. Mater.* **35**, 2107325 (2022).
23. Kumar, P. et al. Photonically active bowtie nanoassemblies with chirality continuum. *Nature* **615**, 418–424 (2023).
24. Kim, R. M. et al. Enantioselective sensing by collective circular dichroism. *Nature* **612**, 470–476 (2022).
25. Lee, H. E. et al. Amino-acid- and peptide-directed synthesis of chiral plasmonic gold nanoparticles. *Nature* **556**, 360–364 (2018).
26. Soukoulis, C. M. & Wegener, M. Past achievements and future challenges in the development of three-dimensional photonic metamaterials. *Nat. Photonics* **5**, 523–530 (2011).
27. Wu, Z., Chen, X., Wang, M., Dong, J. & Zheng, Y. High-performance ultrathin active chiral metamaterials. *ACS Nano* **12**, 5030–5041 (2018).
28. Gansel, J. K. et al. Gold helix photonic metamaterial as broadband circular polarizer. *Science* **325**, 1513–1515 (2009).
29. Han, Z., Wang, F., Sun, J., Wang, X. & Tang, Z. Recent advances in ultrathin chiral metasurfaces by twisted stacking. *Adv. Mater.* **35**, 2206141 (2023).
30. Zhu, A. Y. et al. Giant intrinsic chiro-optical activity in planar dielectric nanostructures. *Light Sci. Appl.* **7**, 17158 (2018).
31. González-Rubio, G. et al. Micelle-directed chiral seeded growth on anisotropic gold nanocrystals. *Science* **368**, 1472–1477 (2020).
32. Mark, A. G., Gibbs, J. G., Lee, T. C. & Fischer, P. Hybrid nanocolloids with programmed three-dimensional shape and material composition. *Nat. Mater.* **12**, 802–807 (2013).
33. Zhao, Y. et al. Chirality detection of enantiomers using twisted optical metamaterials. *Nat. Commun.* **8**, 14180 (2017).
34. Tang, Y. & Cohen, A. E. Optical chirality and its interaction with matter. *Phys. Rev. Lett.* **104**, 1–4 (2010).

35. Yin, X., Schäferling, M., Metzger, B. & Giessen, H. Interpreting chiral nanophotonic spectra: The plasmonic Born-Kuhn model. *Nano Lett.* **13**, 6238–6243 (2013).
36. Kwon, J., Park, K. H., Choi, W. J., Kotov, N. A. & Yeom, J. Chiral spectroscopy of nanostructures. *Acc. Chem. Res.* **56**, 1359–1372 (2023).
37. Khaliq, H. S., Nauman, A., Lee, J. W. & Kim, H. R. Recent progress on plasmonic and dielectric chiral metasurfaces: fundamentals, design strategies, and implementation. *Adv. Opt. Mater.* **11**, 1–24 (2023).
38. Feng, W. et al. Assembly of mesoscale helices with near-unity enantiomeric excess and light-matter interactions for chiral semiconductors. *Sci. Adv.* **3**, 3 (2017).
39. Bae, W. K. et al. R/G/B/Natural white light thin colloidal quantum dot-based light-emitting devices. *Adv. Mater.* **26**, 6387–6393 (2014).
40. Fu, Y. et al. Excellent stability of thicker shell CdSe@ZnS/ZnS quantum dots. *RSC Adv.* **7**, 40866–40872 (2017).
41. Won, Y. H. et al. Highly efficient and stable InP/ZnSe/ZnS quantum dot light-emitting diodes. *Nature* **575**, 634–638 (2019).
42. Choi, M. J. et al. Cascade surface modification of colloidal quantum dot inks enables efficient bulk homojunction photovoltaics. *Nat. Commun.* **11**, 103 (2020).
43. Li, H., Wang, J., Liu, H., Zhang, H. & Li, X. Zinc oxide films prepared by sol-gel method. *J. Cryst. Growth* **275**, 943–946 (2005).
44. Hansen, C. M. *Hansen Solubility Parameters A User's Handbook*. (CRC Press, Taylor & Francis Group, 2018).
45. Mark, J. *Polymer Data Handbook*. (Oxford University Press, 2009).

Acknowledgements

G.Y.K. acknowledge the support from Basic Science Research Program through the National Research Foundation of Korea (NRF) funded by the Ministry of Education (2021R1A6A3A13044445). G.Y.K. and Y.S.J. acknowledge the support from Nano·Material Technology Development Program of the NRF funded by the Ministry of Science and ICT (2021M3H4A3A01062963) and from the NRF funded by the Ministry of Science, ICT (2022R1A2B5B02001743). S. K. and M. S. J. acknowledge the support by the Ministry of Trade, Industry & Energy (MOTIE, 1415180303) and the Korea Semiconductor Research Consortium (KSRC, 20019357).

Author contributions

G.Y.K. and Y.S.J. conceived the project. G.Y.K. conducted mTP development and characterization of QD-based nanostructures. S.K. and M.S.J. performed the numerical analysis of the optical properties of the structures. K.H.P. and J.Y. analyzed the experimental CD data. G.Y.K., Y.S.J., S.K., M.S.J., and M.-J.C. wrote the manuscript. H.J., M.K., T.W.N., K.M.S., H.S., Y.P., and, Y.C. contributed to the discussion and the revision of the manuscript.

Competing interests

The authors declare no competing interests.

Additional information

Supplementary information The online version contains supplementary material available at https://doi.org/10.1038/s41467-024-51179-y.

Correspondence and requests for materials should be addressed to Min-Jae Choi, Min Seok Jang or Yeon Sik Jung.

Peer review information *Nature Communications* thanks Zhiyong Tang, Joel Yang and the other anonymous reviewer(s) for their contribution to the peer review of this work. A peer review file is available.